UFMTrack: Under-Flow Migration Tracker enabling analysis of the entire multi-step immune cell extravasation cascade across the blood-brain barrier in microfluidic devices

Mykhailo Vladymyrov[1, 2], Luca Marchetti[1], Sidar Aydin[1, +], Sasha Soldati[1], Adrien Mossu[1], Arindam Pal[1, Δ], Laurent Gueissaz[1, ◊], Akitaka Ariga[3, □], and Britta Engelhardt[1]

[1] Theodor Kocher Institute, [2] Data Science Lab, and [3] Laboratory for High Energy Physics, University of Bern, Bern, Switzerland

present address: [+] Department of Pharmacology, University of California, San Diego; [Δ] Department of Biomedical Engineering, University of Texas at Dallas; [◊] Department of Neuroscience, Karolinska Institutet, Stockholm, Sweden; [□] Laboratory for Elementary Particle Physics, Department of Physics, Chiba University, Chiba, Japan

Correspondence:

Dr. Mykhailo Vladymyrov

Theodor Kocher Institute

University of Bern, Bern, Switzerland

mykhailo.vladymyrov@tki.unibe.ch

Authors contribution

M.V. implemented the ^{UFM}Track software framework, conducted automated analysis and performance evaluation, and contributed to experimental design and imaging.

M.V. and B.E. wrote the manuscript with contributions from S.S., S.A., and L.M.

M.V., with contributions from S.A., L.M., and S.S., conceptualized the T-cell migration analysis pipeline.

L.M., S.A., and S.S. conducted wet lab experiments and imaging.

S.A., L.M., A.M., and M.V. performed annotation of the datasets for the segmentation model training.

S.A., L.G., A.P., and M.V. performed manual data analysis.

A.A. and B.E. designed the research together with M.V., acquired funding, and coordinated the collaboration.

Abstract

The endothelial blood-brain barrier (BBB) strictly controls immune cell trafficking into the central nervous system (CNS). In neuroinflammatory diseases such as multiple sclerosis, this tight control is, however, disturbed, leading to immune cell infiltration into the CNS. The development of in vitro models of the BBB combined with microfluidic devices has advanced our understanding of the cellular and molecular mechanisms mediating the multi-step T-cell extravasation across the BBB. A major bottleneck of these in vitro studies is the absence of a robust and automated pipeline suitable for analyzing and quantifying the sequential interaction steps of different immune cell subsets with the BBB under physiological flow in vitro.

Here we present the Under-Flow Migration Tracker (^{UFM}Track) framework for studying immune cell interactions with endothelial monolayers under physiological flow. We then showcase a pipeline built based on it to study the entire multi-step extravasation cascade of immune cells across brain microvascular endothelial cells under physiological flow in vitro. ^{UFM}Track achieves 90% track reconstruction efficiency and allows for scaling due to the reduction of the analysis cost and by eliminating experimenter bias. This allowed for an in-depth analysis of all behavioral regimes involved in the multi-step immune cell extravasation cascade. The study summarizes how ^{UFM}Track can be employed to delineate the interactions of $CD4^+$ and $CD8^+$ T cells with the BBB under physiological flow. We also demonstrate its applicability to the other BBB models, showcasing broader applicability of the developed framework to a range of immune cell-endothelial monolayer interaction studies. The ^{UFM}Track framework along with the generated datasets is publicly available in the corresponding repositories.

Author summary

Immune cells continuously travel through our body to perform immune surveillance. They travel within blood vessels at a very high speed and slow down upon reaching their target organ by the

sequential interaction with different adhesion and signaling molecules on the vascular endothelial cells.

The study of molecular mechanisms mediating this multi-step extravasation of immune cells has been significantly advanced by in vitro cultures of microvascular endothelial cell monolayers. The dynamic interaction of the immune cells with endothelial monolayers can be imaged over time in vitro in microfluidic devices under physiological flow. The 2-dimensional structure of the endothelial monolayer allows for reliable visualization of the extravasation process required for the study of the molecular mechanisms involved. The manual analysis of the acquired imaging data is time-consuming and prone to experimenter error. Analysis automation is, however, hampered by the similar appearance of the unlabeled immune and endothelial cells and by the flow causing rapid immune cell displacement.

Here we introduce ^{UFM}Track, the under-flow migration tracker framework allowing for automated analysis of immune cell interactions with microvascular endothelial cells under flow in vitro. ^{UFM}Track performs comparably to the manual analysis of an experienced researcher, eliminates experimenter's bias, and improves the accuracy of the immune cell tracking. Taken together, ^{UFM}Track sets the stage for scalability of in vitro live cell imaging studies of immune cell extravasation.

Keywords

Automated analysis, blood-brain barrier, cell tracking under flow, deep learning, flow chamber, leukocyte trafficking, live cell imaging, machine learning, microfluidics, multiple sclerosis, T cell

Introduction

Immune cells continuously travel throughout our body as a means of immune surveillance. Moving within the bloodstream allows for their fast transport to even distant sites but requires extravasation once they have reached their target organ. Immune cell extravasation across the vascular wall is a multi-step process regulated by the sequential interaction of different signaling and adhesion molecules on the endothelium and the immune cells (1,2). These molecular interactions mediate distinct sequential steps, namely tethering and rolling to reduce travel speed, shear-resistant arrest, polarization and crawling of the immune cell on the luminal surface of the endothelium, and finally, immune cell diapedesis across the endothelial layer (2–4).

The precise molecular mechanisms mediating the multi-step immune cell extravasation in each organ depend on the immune cell subset but also the specific characteristics of the vascular bed. For example, in the central nervous system, the endothelial blood-brain barrier (BBB) establishes a tight barrier that strictly controls the transport of molecules across the BBB, ensuring tissue homeostasis required for neuronal function (2,5). The BBB similarly controls immune cell trafficking into the CNS. Thus, accounting for these special barrier properties, unique characteristics of the multi-step T-cell migration across the BBB have been described. For instance, T cells crawl for very long distances against the direction of blood flow on the surface of the BBB endothelium in search of permissive locations for diapedesis (6–8). Research on T-cell interaction with the BBB has already been successfully translated into therapies in the clinic (9,10).

Exploring the entire multi-step extravasation of immune cells across the BBB has been significantly advanced by making use of in vitro BBB models maintaining their barrier properties, and placing them into microfluidic devices (11). Combined with microscopic setups that allow for in vitro live-cell imaging (Figure 1A-B) of the immune cell interaction with the brain endothelial monolayer under physiological flow over time, the molecular mechanisms mediating the sequential interaction of T cells during extravasation across the BBB have been delineated (2). The live cell imaging is

108 largely performed in the phase-contrast imaging modality (Figure 1C), which does not require
109 establishing fluorescent labels of the imaged cells and avoids potential photo-toxicity of the
110 fluorescent imaging modality. These studies have shown that upon their arrest, T cells polarize and
111 either crawl at speeds between 3 to 10 µm/minute over the brain endothelial monolayer or probe
112 the endothelial monolayer by remaining rather stationary and sending cellular protrusions into the
113 endothelial monolayer (Figure 1D) (12,13). Both behaviors can lead to diapedesis of the T cells across
114 the brain endothelial monolayers. This process lasts at least 3 to 5 minutes, with some immune cells
115 observed to protrude and retract several times prior to finalizing a prolonged diapedesis process to
116 the abluminal side of the brain endothelial monolayer (8,14). Finally, T cells that have successfully
117 migrated across the brain endothelial monolayer usually continue to migrate underneath the
118 endothelial monolayer (15,16).

119 The data analysis of these "in vitro flow assays" requires time-consuming offline frame-by-frame
120 analysis of the imaging data by individual experimenters, in which the dynamic interactions of each
121 individual immune cell has to be followed over the entire time of the assay manually and assigned to
122 specific categories. Such analysis is tedious, and accurately assigning the different T-cell behaviors
123 requires experience. Thus, this manual analysis is prone to inevitable errors and subjective
124 judgments of the various experiments. Furthermore, the time-consuming manual T-cell tracking
125 limits the number of events that can be studied and, thus, the statistical power of the analysis.

126 Automation of the analysis of the recorded multi-step T-cell extravasation across the BBB in the
127 microfluidic device would thus be highly desirable. It is, however, hampered as these assays are
128 usually performed with unlabeled cells and imaged by phase contrast (Figure 1C), which poses a
129 challenge due to the similar grayscales and morphology of the immune cells interacting with the
130 brain endothelial cells. Further challenges include perfused on top T cells that, in the presence of
131 shear flow, instantly appear within the field of view (FoV) and are either suddenly displaced over a
132 certain distance or completely detached and washed away (Figure 1D). Proper analysis of these

events is mandatory for reliable T-cell tracking but also with respect to the study of the overall avidity of the dynamic T-cell interaction steps with the underlying brain endothelium. Thus, it was compulsory to establish a tracking solution that accounts for the effect of the flow on the migrating cells and the distinct migration regimes.

Segmenting of cells imaged in phase contrast migrating on top of cellular monolayer of similar appearance is a challenging task. Furthermore, the analysis of T cell interactions requires detection and quantification of the transmigration. While recent advances in computer vision established several frameworks for detection (17–20) or segmentation (21,22), no tool is readily available to complete both tasks simultaneously.

There is a large number of powerful cell tracking solutions developed that focus on different aspects of cell migration, and are embedded in different frameworks or solutions. The general-purpose Trackpy (23) allows for simple particle tracking and is not suitable to track cells migrating under flow. It is used for the tracking of cells imaged in phase contrast in the Usiigaci framework (24). The widely used TrackMate (25) plugin for ImageJ (26) allows for tracking of particles performing either the Brownian motion or a linear motion, but not the combination of two. Instant appearance or disappearance as well as the resolving tracks of under-segmented cells cannot be easily established in this framework. Similarly, CellTraxx (27) performs matching of cells in the adjacent frames, prohibiting it's use for tracking of under-segmented, intersecting cells or under flow. The Bayesian Tracker (btrack) framework (28) is using spatial information as well as appearance information for track linking focusing on the cell divisions required for cell lineage tracing.

Here we introduce the developed under-flow migration tracker (^{UFM}Track) framework that systematically addresses the hurdles mentioned above, allowing it to perform automated tracking and analysis of cell-cell interactions imaged in phase contrast. We also show a successful implementation of ^{UFM}Track to build an analysis pipeline for T-cell interactions with brain

158 microvascular endothelial cells in vitro under physiological flow. ^{UFM}Track reaches 90% T-cell tracking
159 efficiency, performing comparably to manual analysis while eliminating the experimenter's bias and
160 improving the accuracy of T-cell tracking. Therefore, it enables significant savings in the labor force
161 and time for data analysis.

162

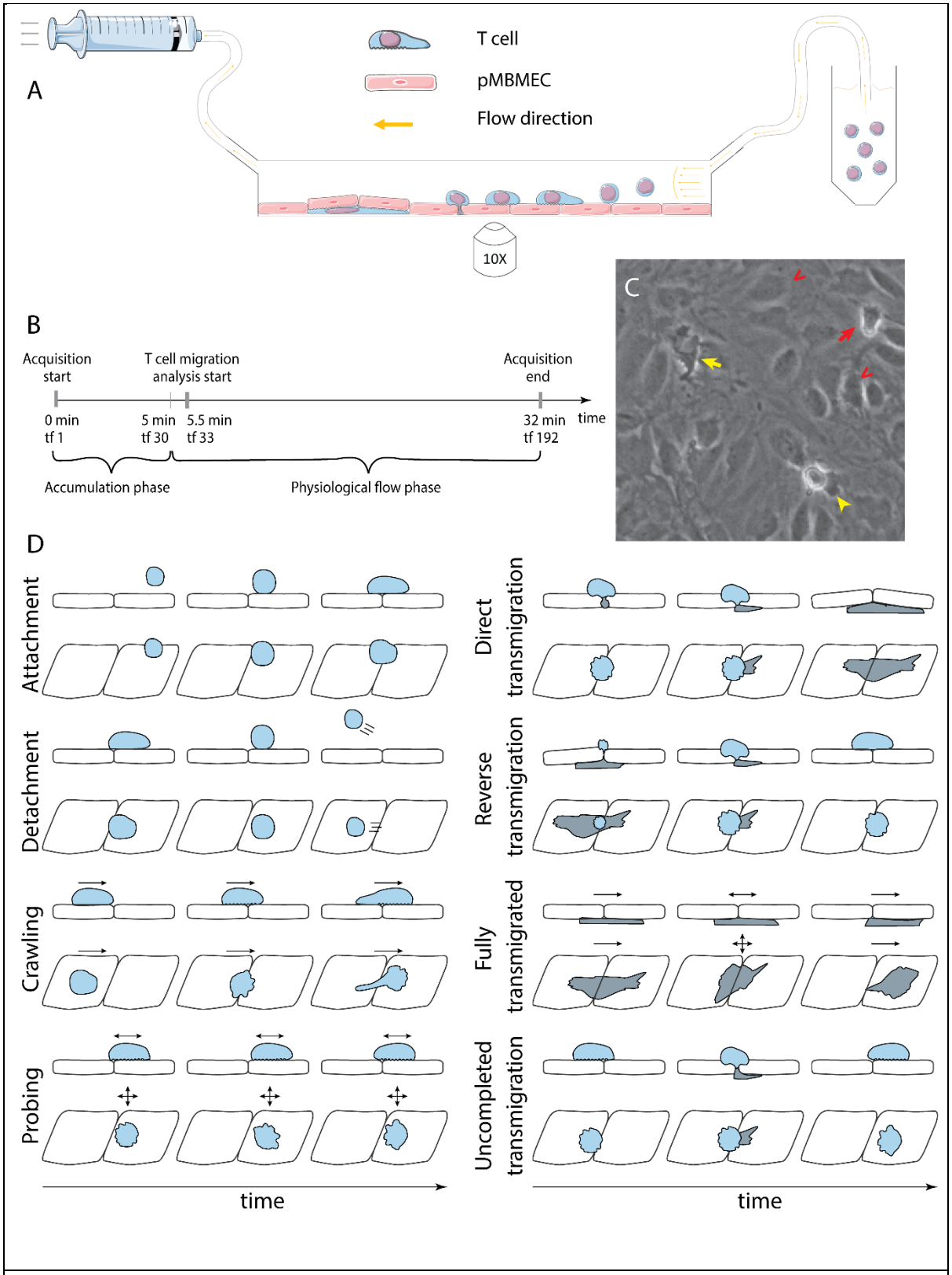

Figure 1. In vitro analysis of the multistep cascade of T-cell migration across the BBB model under physiological flow. A. In vitro under-flow assay setup. T cells were perfused on top of the pMBMEC monolayer, and their migration under flow was observed using phase-contrast imaging modality.

Imaging was performed with a time step of 10 seconds/timeframe. B. In vitro flow assay timeline. During the accumulation phase under flow with the shear stress of 0.1 dynes/cm^2, T cells adhered to the pMBMEC monolayer. After 5 minutes (timeframe 30), the shear stress was increased to 1.5 dynes/cm^2, leading to rapid detachment of not firmly adhering T cells. Analysis of the post-arrest T-cell behavior was thus starting at 5.5 minutes (timeframe 33). tf = timeframe. C. Example of phase-contrast imaging data. Red arrow – crawling T cell; yellow arrow – fully transmigrated T cell; yellow arrow-head – transmigrated part of a partially transmigrated T cell; red V arrowheads – pMBMECs. D. Schematic representation of distinct T-cell behavior regimes detected and analyzed using the developed ^{UFM}Track framework. Crawling cells migrate continuously while probing cells interact with the pMBMECs and move around the interaction point within two cell-size ($20\ \mu m$) as indicated by the arrows. Side and top views are shown.

Results

To design and develop the automated T-cell under-flow migration analysis framework ^{UFM}Track framework presented here, we made use of in vitro imaging datasets following T-cell migration across primary mouse brain microvascular endothelial cells (pMBMECs) under physiological flow in vitro. The framework combines three components: T-cell segmentation and transmigration detection, T-cell tracking under flow, and analysis of each of the multistep T-cell migration cascade steps. Segmentation and transmigration detection of the T cells, migrating on the pMBMECs, is performed with a 2D+T U-Net-like convolutional neural network (21). The T-cell under-flow tracking algorithm was formulated as a constrained optimization problem.

Next, we describe the methods and algorithms employed to develop ^{UFM}Track. Links to the code and the datasets used for model training can be found in the Data Availability section.

176

177 I. T-cell segmentation

178 Reliable cell segmentation is crucial for reliable cell tracking. In the phase-contrast imaging
179 modality, it was impossible to achieve reliable differentiation between T cells and endothelial cells of
180 the pMBMEC monolayer based on pixel intensity. For detection of T-cell transmigration across
181 pMBMEC monolayers (diapedesis), sufficiently reliable cell segmentation of the transmigrated T cells
182 was also required. To achieve this, we have designed 2D and 2D+T U-Net-like (21) fully convolutional
183 neural network-based models for multitask learning. The models were trained to predict three
184 maps: cell probability, the probability that the T cell is below the pMBMEC monolayer, and cell
185 centroids. The models performed predictions based on the grayscale of the respective phase-
186 contrast images in the case of the 2D model or sequences of 5 timeframes in the case of the 2D+T
187 model. The models were implemented in TensorFlow (29). The training was performed on a dataset
188 corresponding to 154 Megapixels of raw image data using the annotation mask for T cells ("T cell
189 mask") and the mask of the transmigrated part of the T cells ("transmigration mask"), the centroids
190 map, and the weight map (Figure 2). For validation 37 Megapixels of raw imaging data were used.
191 The models have approximately 3M and 8M parameters correspondingly, and the model
192 architectures are summarized in Supplementary Tables 1, 2. Details on models' implementation,
193 training, and image processing can be found in the "Segmentation models" section of the
194 Supplementary Material.

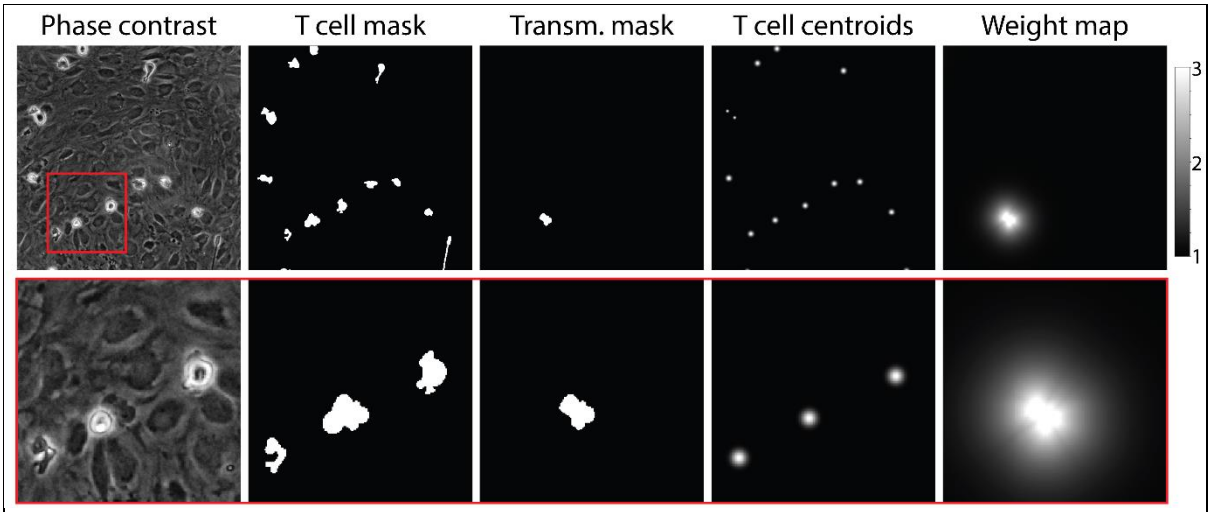

Figure 2. Example of data used for training of the T-cell segmentation model. From left to right: Phase-contrast microscopy image of T cells migrating on top of the pMBMEC monolayer; annotated T cell mask; annotated mask of transmigrated part of T cells; T cell centroids; w_{cell} weight map. The bottom row shows zoom-in on the highlighted area.

In the T cell mask prediction task, the 2D+T model outperformed the 2D model by a notable 9% according to the average precision (AP) metric (Table 1). At the same time, for the transmigration mask, which is much more difficult to infer, the 2D model performance reached only 54%, which is insufficient for reliable detection of T cells migrating across the pMBMEC monolayer. In this task, the 2D+T model outperformed the 2D model by 32% AP. We observed that the 2D+T model was sensitive to frame misalignment, leading to false positive detection of transmigrated T cells. Thus, to generate the preliminary T-cell masks used for frame alignment and histogram normalization, we employed the 2D model. Afterward, for the T-cell segmentation and transmigration detection, we employed the 2D+T model, followed by a watershed algorithm based on the inferred T-cell mask and the cell centroids as seed points. A stitched phase-contrast image sequence can be seen in Supplementary Video 1 and overlayed with the segmented cells and highlighted transmigration mask in Supplementary Video 2.

Table 1. Comparison of the performance of the 2D and 2D+T-cell segmentation models.

	Performance, AP	
	2D	2D+T
T Cell mask	86.12%	95.26%
Transmigration mask	50.56%	82.74%

After segmentation, we suppressed the noise by discarding small objects with an area below 30 pixels (the mean area of a T cell is about 400 pixels). For each T cell, we evaluated its coordinates as geometric mean coordinate, angle of the longer axis, and elongation $\epsilon = \sqrt{\frac{\sum_i (x_i' - x_0')^2}{\sum_i (y_i - y_0')^2}}$,where x_i', y_i' are projections of the i-th T cell mask pixel coordinates on the orthogonal long and short axes of the T cell, and x_0', y_0' are the corresponding projections of the geometrical center of the T cell. The summation is performed over the area covered by the mask of the corresponding T cell. Additionally, we evaluated the mean T cell probability $\overline{p_{cell}} = \frac{1}{n_{pix}} \sum_i p_{cell,i}$, mean transmigration probability $\overline{p_{tr}} = \frac{1}{n_{pix}} \sum_i p_{tr,i}$, and cell transmigration coefficient as $t_c = \frac{1}{n_{pix}} \sum_i \frac{\min(p_{tr,i},\ p_{cell,i})}{p_{cell,i}}$, where n_{pix} is number if cell pixels and $p_{cell,i}$, $p_{tr,i}$ are the T cell and transmigration probabilities for i-th pixel in the predicted T cell mask.

II. T-cell tracking

The presence of flow causes several types of discontinuous events that were managed with a specialized tracking algorithm. These are: 1) the sudden appearance of T cells in the field of view (FoV), 2) the sudden detachment of a T cell followed by its disappearance from FoV, and 3) the displacement over significant distances (up to hundreds of micrometers) of T cells that do not

227 adhere firmly to the pMBMECs. The primary inspiration for our approach was the Conservation
228 Tracking algorithm (30). We could consistently reconstruct the T-cell tracks by performing global
229 optimization constrained to controlled probabilities of T-cell appearance, disappearance, and
230 displacement due to the flow at every time point. The standard tracking algorithms like tracking by
231 association is either unable to detect track links with high displacement and thus reconstructs
232 several disconnected segments of a cell track, or leads to a high number of false track links. Our
233 procedure favors the reconstruction of long T-cell tracks while at the same time allowing for tracking
234 of the T cells which detach or are displaced by the flow ("accelerated T-cell movement") over a
235 longer distance ($> 8\ \mu m$) with speed significantly higher than their crawling speed.

236 The tracking consists of four main steps: linking, searching for track candidates, global track
237 consistency resolving, and resolving the track intersections. The inputs for the tracking are the
238 segmented cells and the cell centroids (Figure 3A). The centroids and the cell proximity are used to
239 quantify under-segmentation by introducing the node multiplicity (Figure 3B, see section T-cell
240 tracking of the supplementary information for details). At the linking step, we identified all possible
241 connections of T cells between the timeframes (Figure 3C).

242 Next, during the search for track candidates, we aimed to find continuous track segments of T
243 cells or under-segmented groups of T cells crawling on top of or below the pMBMEC monolayer
244 without accelerated movement segments on the T cell track characterized by rapid T cell
245 displacements. The whole dataset of T cells across all time points was represented as a graph. Each
246 vertex corresponds to a T cell (multiplicity m=1) or a group of potentially under-segmented T cells
247 (m>1). The vertices are connected according to links obtained at the linking step. Track segments
248 were found by performing global optimization to find consistent connectivity of vertices across the
249 time points (Figure 3D) by employing an approach inspired by the conservation tracking algorithm
250 summarized in Schiegg et al. (30). Optimization was performed using the CP-SAT constrained
251 optimization procedure using the open source OR-Tools library (31).

Next, resolving global track consistency was performed. In this step, the scope of T cell tracking is shifted from individual nodes (representing T cells at particular timeframes as well as groups of under-segmented T cells) to the track segments (unambiguous sequences of nodes) and vertices at the endpoints of the segments. These are track start and end points, points of merging and separation of track segments in case of under-segmentation, as well as ambiguous points on a track. The latter was identified by sudden T cell displacement, a hallmark of detaching and reattaching T cells and T cells transitioning from properly segmented to under-segmented T cells or vice versa (Figure 3E). This was followed by the search for potential missing track segments due to accelerated T cell movement under flow and missing links in the track crossing points. Both are characterized by significant displacement lengths such that they were not detected during the linking step. Thus we will refer to both as "jumps" in this section. We have also eliminated short and therefore unreliable segments, as well as segments whose multiplicity was found to be $M = 0$ (Figure 3F). Afterward, we separated the segments into two categories, namely segments with multiplicity $M = 1$, i.e., tracks of isolated T cells, and segments with multiplicity $M > 1$, i.e., tracks of under-segmented groups of T cells, where tracks of several T cells intersected. Finally, we extended the tracks of isolated T cells into the intersection if the branching vertex had a multiplicity of n and was splitting in exactly n segments with multiplicity $M = 1$ (Figure 3G).

Lastly, we resolved the track intersections to obtain reliable T cell tracks, i.e., identifying track segments corresponding to the same T cell before and after the under-segmented track region (Figure 3H).

Detailed information on the developed under-flow T cell tracking algorithm is given in the "T-cell tracking" section of the Supplementary Material.

III. T-cell migration analysis

Next, we performed the T-cell migration analysis based on the reconstructed T cell tracks. We selected tracks inside the fiducial area of the FoV, namely coordinates of the T cell at all timepoints

277 along the track were located at least 25 µm away from the bounding box enclosing all segmented T
278 cells. Next, tracks of T cells touching another T cell at the end of the assay acquisition were excluded
279 since T cells directly adjacent to each other can hide the start of T cell transmigration across the
280 pMBMEC monolayer and thus compromise correct detection and quantification of this step.
281 Additionally, only tracks with T cells were assigned in at least 6 timeframes during the physiological
282 flow phase. We also require T cells to be assigned for at least 75% of timeframes along the track.
283 Under-segmented parts of T cell tracks were not considered. Examples of selected tracks can be
284 seen in Supplementary Video 3.

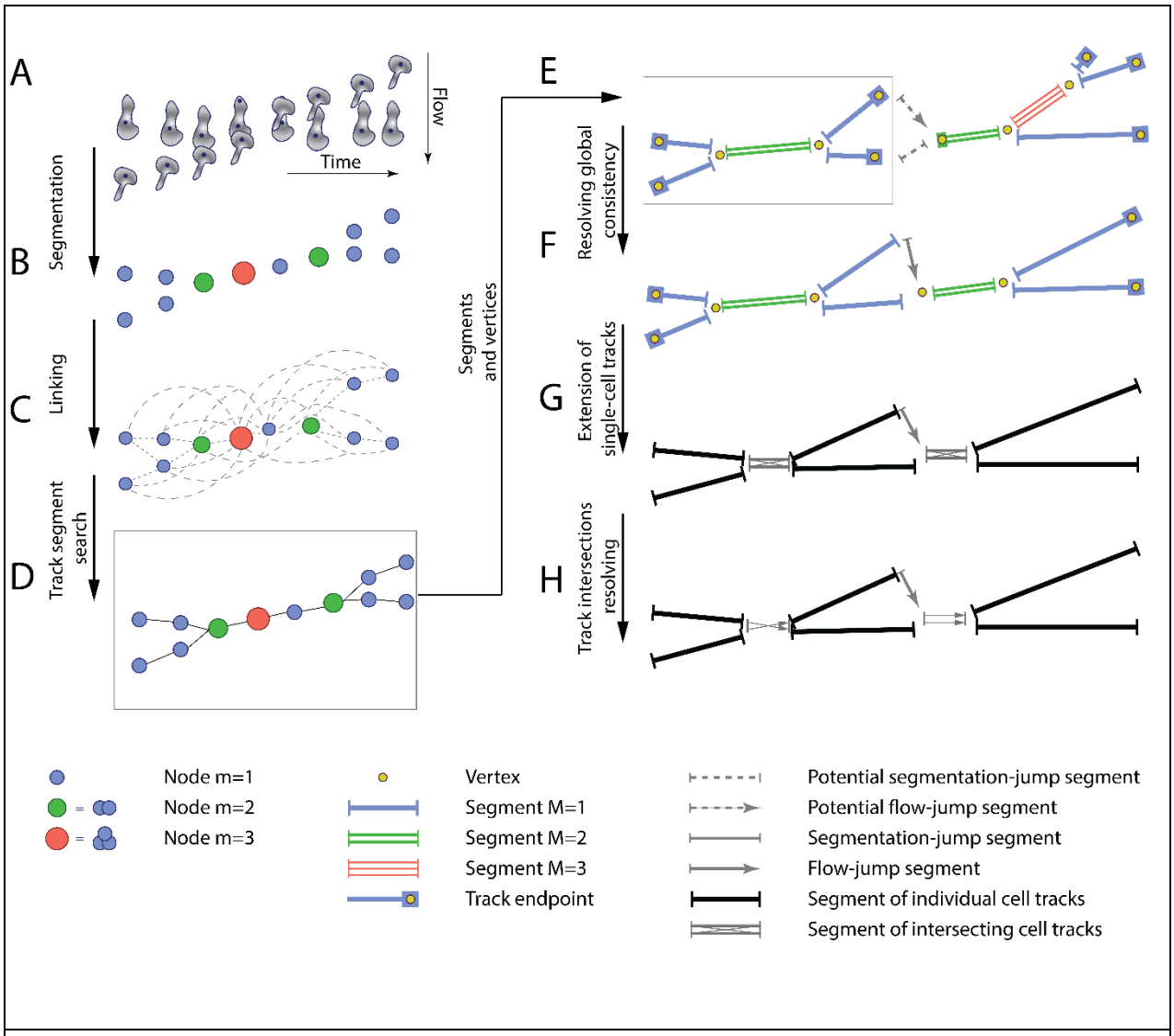

Figure 3. The T-cell tracking pipeline. A. Segmentation and centroids of two migrating T cells under flow over time. B. Nodes corresponding to segmented T cells. Node sizes and colors denote the multiplicity

estimate of a node. C. Nodes, together with links between adjacent in space and time nodes, form a graph. D. Selected links are obtained with global optimization on the graph. E. Graph of segments and vertices obtained according to node multiplicity. F. Resolving global segment multiplicity consistency with global optimization on the graph. Additionally, a search for rapid displacement of segmented T cells due to under-segmentation or flow is performed. G. Extension of tracks of individual T cells into the track intersection. H. Resolving track intersections.

After exclusion of the tracks of the cellular debris, which were misclassified as T cells during the segmentation step, using a dedicated “not-a-T-cell” classifier, we performed identification of transmigration (Supplementary Figure 5), probing and crawling migration regimes, as well as accelerated movement along the T cell track. Detailed information on the analysis of the T cell tracks is given in the “T-cell migration analysis” section of the Supplementary Material.

Finally, for each track, we evaluated motility parameters for each of the following migration regimes: probing before the transmigration, crawling before the transmigration, all crawling above pMBMECs monolayer including T cell crawling segments after the first transmigration attempts, all crawling below pMBMECs monolayer, whole T-cell track excluding accelerated movement and tracking inefficiency regions, as well as whole T-cell track. Specifically, we evaluated the following T-cell motility parameters: duration of each migration regime, the total vector and absolute displacements, the migration path length, the average migration speed (displacement over time), average crawling speed (path length over time), and finally the mean and standard deviation of the instantaneous speed. We evaluated migration time, displacement, and average speed for the accelerated movement regime.

IV. Analysis of trafficking datasets

303 Having developed a full pipeline based on the UFMTrack framework for automated analysis of the
304 multi-step T-cell migration cascade across the BBB model, we next aimed to compare the results of
305 the automated analysis with previous studies, assess the capacity of the framework to gain novel
306 insight into T-cell migration under flow, and evaluate its performance as compared to manual
307 analysis.

308

309 1. $CD4^+$ T cell analysis

310 To this end, we first analyzed a total of 18 imaging datasets each corresponding to 32 minutes
311 recording dedicated to understanding the multi-step migration of $CD4^+$ T cells across non-stimulated
312 (n= 6), TNF stimulated (n=5), and IL1-β-stimulated (n=7) pMBMEC monolayers under physiological
313 flow with the developed pipeline.

314 In these in vitro live cell imaging datasets, phase-contrast imaging was performed as described in
315 the "Data acquisition" subsection in the Materials and Methods section. The T-cell accumulation
316 phase corresponding to the shear stress of 0.1 dynes/cm^2 lasted for 32 timeframes (5 minutes),
317 followed by conditions of physiological flow (shear stress 1.5 dynes/cm^2) for the subsequent 160
318 timeframes (27 minutes). The shear stress is controlled by an automated syringe pump. After
319 increasing to physiological flow rates (12), a significant number of T cells detached from the
320 pMBMEC monolayers, with higher numbers of T cells detaching from non-stimulated pMBMEC
321 monolayers when compared to those stimulated with pro-inflammatory cytokines as detected by
322 the distribution of the track ending times between 5 and 30 minutes. (Figure 4A).

323 Analyzing these datasets with the established UFMTrack framework, the T-cell behavior type for
324 each detected T-cell track and the aggregated T-cell behavior statistic were obtained for the
325 stimulated and non-stimulated pMBMEC monolayers (Figure 4B). The total number of analyzed T cell
326 tracks is n=971, n=780, and n=1218 for the non-stimulated, TNF stimulated, and IL1-β stimulated

327 pMBMEC monolayers correspondingly. The data obtained with UFMTrack were in accordance with our
328 previous observations obtained by manual frame-by-frame analysis (12,14,32). We further obtained
329 the data for T-cell migration speed, T-cell displacement, and T-cell path lengths for the crawling T
330 cells, as these are the primary cell motility parameters. As shown in Figure 4C-H, we observed
331 statistically significant differences in the mean T-cell motility parameters depending on the
332 pMBMECs stimulation condition. Furthermore, we observed differences in the shape of the
333 distribution of T-cell crawling speeds, consistent with our previous reports of underlying differences
334 in the mechanisms mediating T-cell crawling on non-stimulated versus cytokine-stimulated
335 pMBMECs (32). While not statistically significant for the IL1-b and with a low significance for the TNF
336 stimulations, an increased variance of the T cell instantaneous speed on stimulated compared to
337 non-stimulated pMBMECs is observed(Figure 4G). This suggests that T-cell crawling is often
338 interrupted by T-cell recognizing specific cues on the stimulated endothelium. The T cell meandering
339 index (MI) distribution was high on non-stimulated and lower on stimulated pMBMECs (Figure 4H),
340 underscoring that cytokine stimulation enhances directed T-cell movement on the pMBMEC
341 monolayer.

342 Since the analysis was performed automatically with UFMTrack, it allowed for deeper insights into
343 the T-cell migration behavior on the pMBMEC monolayers than obtained by manual frame-by-frame
344 analysis. Specifically, the detection of accelerated movement by UFMTrack enables the researcher to
345 quantify the kinetics of individual T-cell detachment from the endothelium rather than simply
346 quantifying a bulk T-cell detachment rate. This detachment kinetics is reflected in the average speed
347 experienced during accelerated movement, which is significantly lower for the IL1-b condition
348 (Figure 4I), suggesting the need to break more bonds with the endothelium when pro-inflammatory
349 cytokines are present.

350 As our UFMTrack workflow achieves sufficient segmentation efficiency to detect T cells below the
351 pMBMEC monolayer and T-cell transmigration across the pMBMEC monolayer, it also enables

352 investigation of T-cell movement after the transmigration step. In Figure 4J, we show the distribution
353 of the migration speed for the transmigrated $CD4^+$ T cells. Interestingly, cytokine stimulation of
354 pMBMECs, although applied from the luminal side, also affected T-cell movement at the abluminal
355 side of the pMBMEC monolayer. While in the microfluidic device used in the present study, the
356 migration of T cells below the pMBMEC monolayer may not be biologically relevant, this analysis
357 option will be valuable for future studies involving multilayer in vitro BBB models that include the
358 vascular basement membrane in addition to pericytes and astrocytes to mimic the entire
359 neurovascular unit (8,33).

360 Importantly, our ^{UFM}Track automatically detects and characterizes unusual events, such as reverse
361 T-cell transmigration, that are easily overlooked with manual counting. We do not present the
362 statistics here, as only a few such events were observed. However, when applied to the multilayer
363 BBBs in forthcoming in vitro models, systematic detection and analysis of these rare events will be
364 important to understand T-cell migration in immune surveillance.

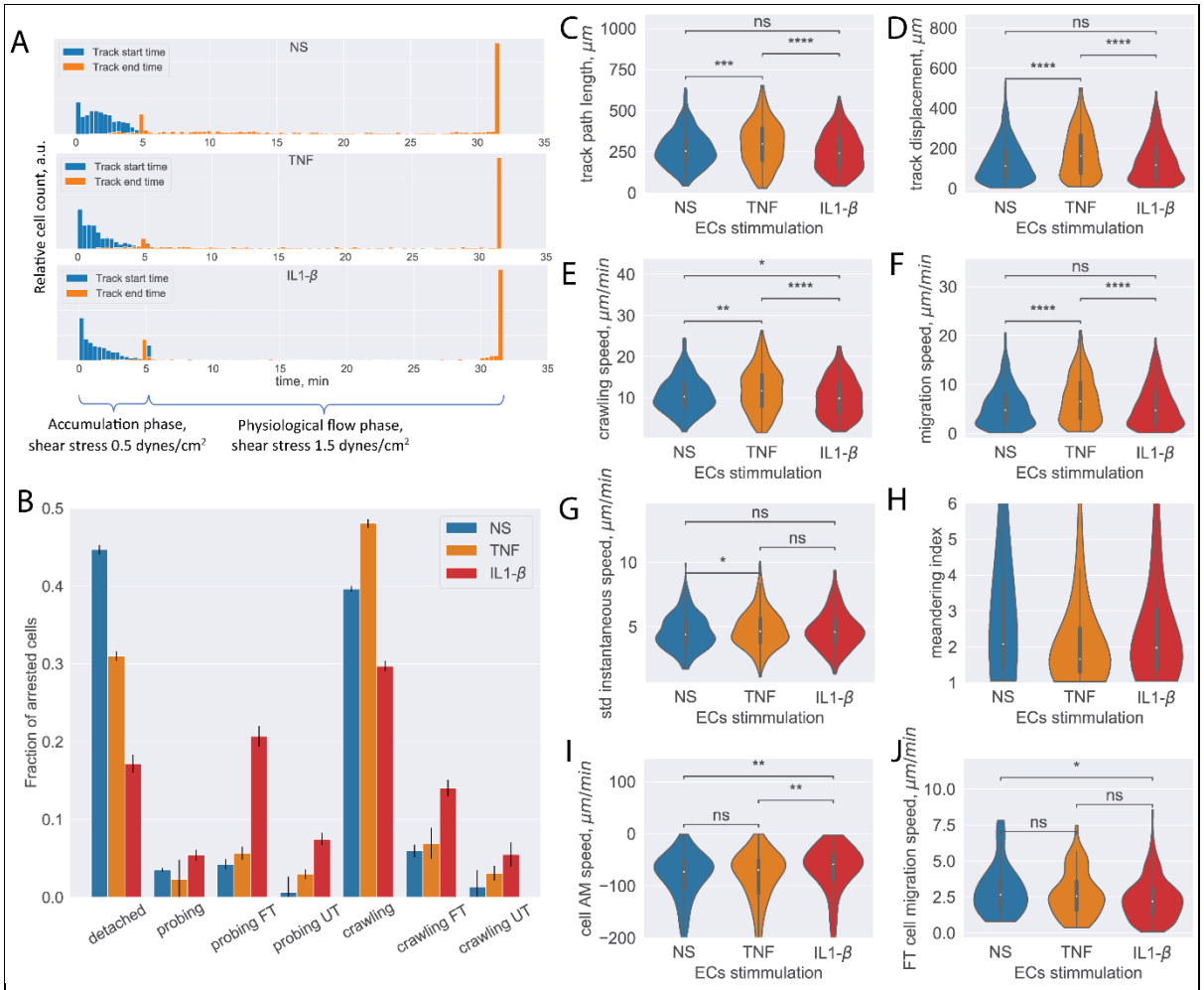

Figure 4. Analysis of CD4⁺ T-cell tracks. A. Start and end time distribution of CD4⁺ T-cell tracks on non-stimulated or TNF or IL-1β stimulated pMBMECs. UFMTrack correctly captures increased T-cell detachment from the non-stimulated pMBMECs after 5 minutes when the flow is increased to physiological levels. B. Quantification of CD4⁺ T-cell behavior in the respective categories obtained on non-stimulated and TNF and IL-1β stimulated pMBMECs. Error bars show the statistical error of the mean. (see text for details). C-H. Motility parameters of the crawling CD4⁺ T cells were obtained for the three endothelial stimulatory conditions. Distributions of T-cell path length (C), displacement (D), crawling speed (path/time) (E), migration speed (displacement/time) (F), variability of instantaneous T-cell crawling speed along the track (standard deviation, G), and meandering index (H). I. Distribution of CD4⁺ T-cell accelerated movement (AM) speed is a proxy

metric for the T-cell adhesion to the healthy or inflamed endothelium. J. Migration speed distribution of the transmigrated $CD4^+$ T cells. Stimulation applied to the luminal side of pMBMECs affects T-cell migration at the abluminal side of pMBMECs after their transmigration.
FT - T cells performed full transmigration; UT – T cells performed uncompleted transmigration.

365

366 2. $CD8^+$ T cells analysis

367 As we have previously shown that the multi-step T-cell extravasation across pMBMEC
368 monolayers differs between $CD4^+$ and $CD8^+$ T cells (13), we next analyzed two datasets studying the
369 multi-step migration of $CD8^+$ T cells across non-stimulated (NS) and TNF/ interferon-gamma
370 (TNF/IFN-γ) stimulated pMBMEC monolayers under physiological flow over 161 timeframes
371 (27 minutes). The $CD8^+$ T cells were slightly different in size and appearance when compared to the
372 $CD4^+$ T cells used for training the segmentation model. To benchmark our established ^{UFM}Track
373 pipeline in this more difficult configuration, the datasets were first manually analyzed by four
374 experimenters: one advanced experimenter with four years of experience (AdEx) and three
375 inexperienced experimenters who received comparable 2-hour introduction and training (Ex1-Ex3).
376 The analyses were performed on the subset of the acquisition, 161 timeframes long starting from
377 timeframe 31.

378 Manual cell analysis and tracking were performed as described in the “Materials and Methods”
379 section separately for each of the 8 tiles of the tiled acquisition. Next, all crawling $CD8^+$ T cells that
380 did not perform transmigration were manually tracked for the timespan after the flow was increased
381 to the physiological level using the manual tracking in ImageJ.

382

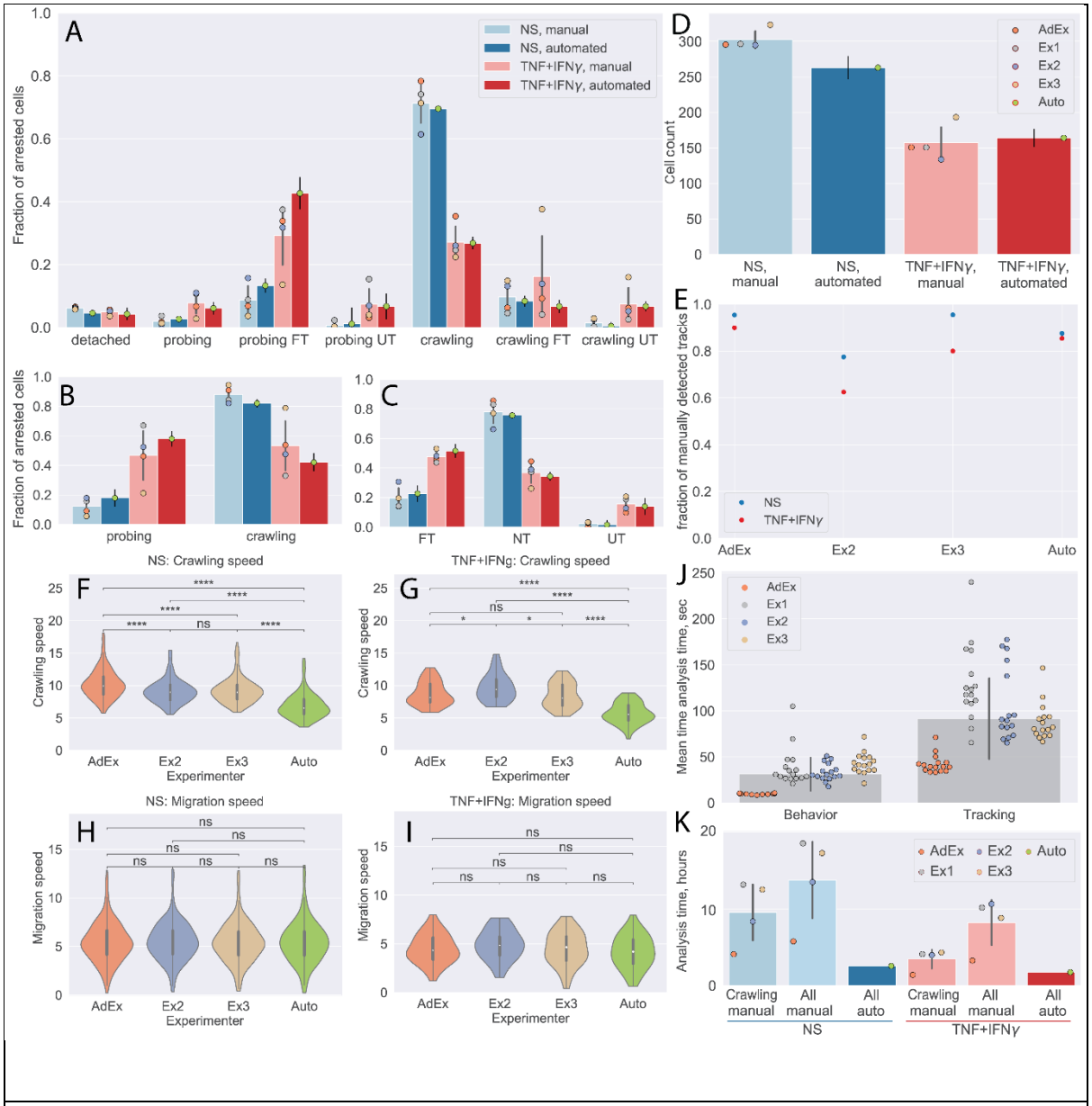

Figure 5. Comparison of automated analysis with ^{UFM}Track and manual analysis of the CD8$^+$ T-cell tracks. A-C: CD8$^+$ T-cell behavior statistic obtained for non-stimulated (NS) and cytokine-stimulated pMBMECs as obtained manually by four experimenters, as well as automatically with ^{UFM}Track. A. Quantification of CD8$^+$ T-cell behavior in the respective categories obtained on non-stimulated and TNF/IFN-γ stimulated pMBMECs is consistent with results obtained by manual frame-by-frame analysis. Cytokine stimulation of pMBMECs increases T-cell probing behavior (B) and T-cell transmigration rate (C). Error bars show the standard deviation of the manual analysis and the statistical error of the mean for automated analysis. Points correspond to individual experimenters.

D. Counts of CD8$^+$ T cells were obtained manually by four experimenters and automatically by ^{UFM}Track. The T-cell detection efficiency is above 90%. Error bars show the standard deviation of the manual analysis and the statistical error of the mean for the automated analysis. Points correspond to individual experimenters. E. Detection efficiency of crawling CD8$^+$ T cell tracks between the manual and automated analysis. F-I. Comparison of CD8$^+$ T-cell crawling speed (path/time) (F, G) and migration speed (displacement/time) (H, I) on non-stimulated (F, H) and cytokine-stimulated (G, I) pMBMECs. The T-cell position assignment error in manual tracking leads to biased crawling speed estimation. J. Comparison of the analysis time (per cell) required for behavior analysis and tracking of CD8$^+$ T cells. K. Total analysis time (per dataset) for behavior analysis and tracking of CD8$^+$ T cells. Comparison is shown for manual analysis with tracking of crawling cells only (Crawling manual), the time estimate for manual analysis with tracking of all cells (All manual), and the in-depth automated analysis of all cell tracks with ^{UFM}Track (All auto).

FT - T cells performed full transmigration; UT – T cells performed uncompleted transmigration; NT - T cells did not perform transmigration.

First, we compared the CD8$^+$ T cell behavior statistics obtained manually and by our automated analysis pipeline (Figure 5A-C). The results obtained by the automated analysis were in full agreement with the manual analysis performed by the experienced experimenter. At the same time, the data highlight the variability of the results from the inexperienced experimenters, confirming the potential for significant experimenter bias.

We also show the detection efficiency of T cells by the ^{UFM}Track. To achieve this goal, we combined the numbers of CD8$^+$ T cells detected in each tile by manual analysis. Due to the overlap between the individual tiles, some CD8$^+$ T cells are seen more than once. To obtain an estimate of the total CD8$^+$ T cell count detected manually, we scaled the number of CD8$^+$ T cells accordingly to the number of detected unique T-cell tracks (see next paragraph). By this approach, we found T-cell detection efficiency to be above 90% (Figure 5D). The increased T-cell density can explain lower

395 efficiency in the NS condition. These findings set the appropriate T-cell density for automated
396 analysis of their migration behavior on pMBMEC monolayers to 200-300 cells per FoV of the size of
397 3.8 mm^2 or 50-80 cells/mm^2.

398 Next, we compared the T-cells tracks as obtained manually by three experimenters as well as
399 automatically by our ^{UFM}Track. To this end, we first matched the tracks in adjacent tiles to obtain the
400 tracks on the whole imaging area, avoiding multiple counts of the same track. This was achieved by
401 pattern matching with initial offsets between tiles obtained by an automatic frame alignment
402 procedure performed as part of the automatic analysis. We considered T-cell tracks observed in
403 different tiles to be tracks of the same T cell if $f_{in} > \frac{1}{2} f_{out} - 0.8$, where f_{in} is the fraction of
404 timepoints along a track at which the distance between the T cells was below 17 µm and f_{out} was
405 the fraction of timepoints along a track at which distance between cells was above 25 µm. We used
406 the same approach to match the T-cell tracks obtained by each experimenter and the automated
407 ^{UFM}Track. To compare performance in an objective manner, we excluded manually obtained tracks
408 that lay outside of the fiducial volume of the automated analysis, as well as T cells that were
409 touching another T cell at the end of the acquisition, as those were also excluded from the
410 automated analysis. We then took as 100% the sum of all T-cell tracks detected manually. We
411 evaluated the fraction of all T-cell tracks detected by each experimenter as well as automatically by
412 our ^{UFM}Track.

413 In Figure 5E, we show that our pipeline achieves a comparable T-cell tracking efficiency when
414 compared to the manual analysis. While its performance was not superior to that of the
415 experimenter with four years of expertise in the analysis of the under-flow datasets, it does perform
416 better than less experienced experimenters.

417 We also compared the T-cell motility parameters obtained manually and automatically for the
418 non-stimulated and stimulated pMBMECs (Figure 5F-I). Data obtained for the $CD8^+$ T-cell migration
419 speed on pMBMECs was comparable between all experimenters and the automated analysis. In

420 contrast, results obtained for the T-cell crawling speed were significantly different between the
421 automated approach and manual analysis. Taking a closer look at the T-cell tracks (Supplementary
422 Figure 6), we readily observed that the manual analysis contains significant errors in the assignment
423 of the T-cell position. This leads to a jittery pattern in the T-cell migration tracks and overestimating
424 the T-cell path and, thus, T-cell crawling speed. Employing our novel automated analysis pipeline
425 eliminated this systematic error in the measurements.

426 To finally investigate the potential benefit in the time required for automated versus manual data
427 analysis, we examined the time required for a given experimenter to analyze such datasets manually
428 using the Clockify time tracker (34). In Figure 5J, we show the average time investment needed to
429 perform a complete T-cell behavior analysis and T-cell tracking in each imaging tile, as well as on
430 average. Clearly, the experienced experimenter outperforms the inexperienced experimenters by a
431 factor of 3. On average, a researcher would thus spend 8.1 hours analyzing a dataset with 300 T cells
432 when only the tracks of crawling T cells (50%, i.e., 150 cells) are analyzed. If all T-cell tracks were to
433 be analyzed, this time would further increase to 12.9 hours. Given that on average 10 datasets can
434 be produced per day, manual analysis becomes a bottleneck, leading to delays in exhaustive data
435 analysis and thus ultimately in research progress. The ^{UFM}Track framework reduces analysis time by a
436 factor of 3 when analyzing only crawling cells and 5 if all cell tracks are to be analyzed (Figure 5K).
437 With an average analysis time of 2.3 hours, the 10 experiments carried out in one day can be
438 thoroughly analyzed within one day of machine time. This enables the scalability of flow-based
439 immune cell migration experiments while simultaneously lifting the burden of tedious and time-
440 consuming manual analysis from the researchers.

441

442 V. Applicability of ^{UFM}Track to different models of immune cell - endothelial cell interactions

443 To assess the broader applicability of the ^{UFM}Track framework to different cell types and BBB
444 models employed for the *in vitro* under-flow cell trafficking assays. To this end, we have performed

445 the automated analysis of the multi-step T-cell migration cascade in a set of datasets (one to eight)
446 across different cell types and assays. Specifically, we attempted to verify the feasibility of analysis of
447 datasets where the cells forming the monolayer or the migrating cells have noticeably different
448 appearances, cells from other species are used, specifically human-derived cells, and datasets with a
449 different imaging modality. These include human peripheral blood mononuclear cells (hPBMCs),
450 human T cells, bone marrow-derived macrophages (BMDM) interacting with a monolayer of mouse-
451 and human-derived brain microvascular endothelial cells as well as with immobilized recombinant
452 BBB adhesion molecules (See "Material and Methods" section for details). To assess the
453 performance of the model in each condition, we have performed a visual inspection of the cell
454 masks, transmigration masks, and cell tracks for few datasets in each assay type. We then analyzed
455 cell behavior distribution or motility parameters relevant in each case.

456

457 1. hPBMC on HBMEC monolayer

458 The interaction of hPBMCs with the BBB is altered under different disease conditions. We have
459 therefore analyzed a dataset of human PBMCs on human brain microvascular endothelial cells
460 (HBMEC) to quantify the cell behavior statistic. While the endothelial cells look significantly different
461 than the pMBMECs, the segmentation and transmigration detection quality was sufficient to
462 perform the cell migration analysis. This was also confirmed by the visual inspection of the cell and
463 transmigration masks and cell tracking results (Figure 6 A). We then quantified the PBMC behavior
464 distribution and the crawling and migration speed of the crawling PBMC (Figure 6 B, C).

465 2. BMDM on the pMBMEC monolayer

466 Invasion of macrophages into the CNS contributes to many neurological disorders. Therefore, we
467 have explored if ^{UFM}Track also allows us to analyze the interaction of BMDMs with the BBB under
468 physiological flow in vitro. To this end, we have analyzed two datasets of mouse BMDMs interacting

469 with pMBMEC monolayers (Figure 6 D). Despite the different behavior and appearance of the
470 macrophages as compared to the T cells, the segmentation quality was sufficient to perform the cell
471 tracking and analyze cell motility parameters (Figure 6 E, F), as confirmed by visual inspection of the
472 macrophages masks and cell tracking results (Figure 6 D). Nonetheless, due to the different
473 appearance of the flattening crawling cells and the transmigrated cells, the transmigration detection
474 trained on the mouse T cells does not perform sufficiently well for the robust detection of
475 transmigrating macrophages.

476 3. Human T cells on EECM-BMEC monolayer

477 Next, we analyzed eight datasets of human T cells interacting with the human induced pluripotent
478 stem cell (hiPSC) derived extended endothelial cell culture method brain microvascular endothelial
479 cell (EECM-BMEC)-like cell monolayers (Figure 6 G). EECM-BMECs establish barrier properties
480 comparable to primary human BMECs and display a mature immune phenotype allowing to perform
481 studies for the first time in a fully autologous manner of immune cell interactions with patient-
482 derived in vitro models of the BBB (35). Despite the cells being of different species, the T cells were
483 successfully segmented, and their transmigration was detected, as confirmed by visual inspection of
484 the T-cell and transmigration masks and cell tracking results (Figure 6 G).

485 We have confirmed the differences in migration statistics (Figure 6 J, K), migration and crawling
486 speed of the crawling T cells (Figure 6 H), as well as the previously reported difference in relative
487 (normalized to track pathlength) displacement (Figure 6 I) of the T cells treated with anti-α4-integrin
488 + anti-β2-integrin blocking antibodies (bab) and control (ctrl) condition (36).

489 4. Human T cells on immobilized recombinant BBB adhesion molecules

490 Finally, we have analyzed datasets acquired in a different imaging modality. Seven datasets of
491 human T cells interacting with immobilized recombinant BBB adhesion molecules, namely ICAM-1,
492 VCAM-1, and their combination (Figure 6 l). In this case, the fluorescently labeled cells were imaged

493 with epi-fluorescent microscopy. In the absence of a monolayer, transmigration detection is not
494 necessary. Thus we performed cell segmentation directly on the fluorescent signal (See Materials
495 and Methods for details) using the same segmentation strategy as for the T-cell masks. The tracking
496 was then performed the same way as for other experiments. The T cells were successfully
497 segmented and tracked, as confirmed by visual inspection. We compared T cell behavior and motility
498 parameters for three conditions of the recombinant adhesion molecules: ICAM-1, VCAM-1, and
499 ICAM1 + VCAM1 (Figure 6 M, O). Consistent with previous observations (12,36) where the analysis
500 was performed using the ImageJ (26) either manually or with the TrackMate (25) plugin, we
501 observed that in the absence of ICAM-1, T cells were moving in the direction of flow (Figure 6 N). At
502 the same time, ^{UFM}Track allows for capturing the rapid accelerated motions of the cells and thus
503 reconstructing longer continuous T cell tracks. This enables capturing the migrations properties of
504 the consecutive steps of the T cell migration cascade on the call-by-cell basis.

505

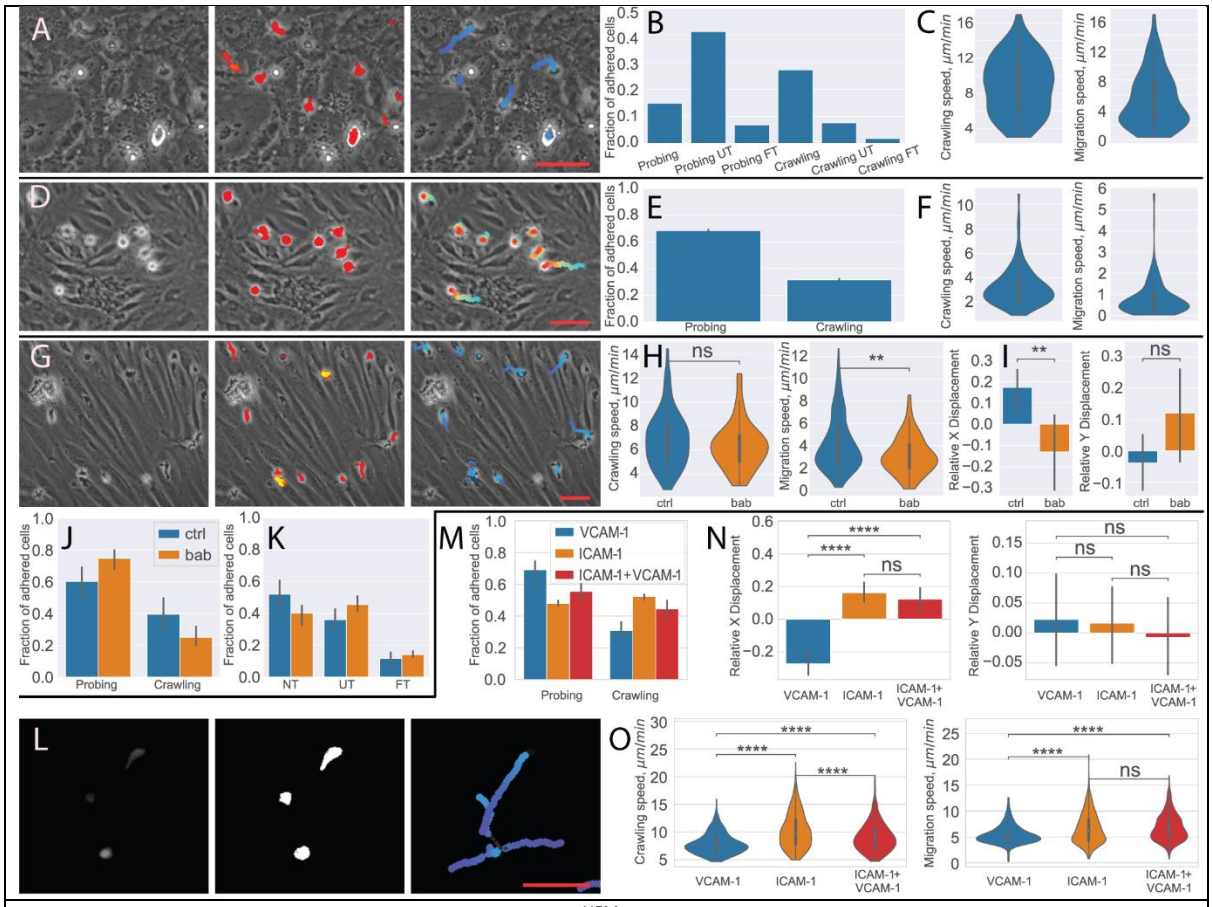

Figure 6. Analysis of different BBB models with UFMTrack. A-C. Human PBMCs interacting with HBMEC. A. Raw image frame, segmentation, and tracking results. B. PBMCs behavior distribution. C. Crawling and migration speed distribution. D-F. BMDM interacting with the pMBMEC monolayer. D. Raw image frame, segmentation, and tracking results. E. BMDM crawling vs probing behavior distribution. F. Crawling and migration speed distribution. G-K. Human T cells interacting with the EECM BMEC monolayer. G. Raw image frame, segmentation, and tracking results. H. Crawling and migration speed distributions for the control condition (ctrl) and with the blocking anti-bodies (bab). I. X and Y relative cell displacement. J. Crawling vs probing behavior comparison. K. Transmigrations behavior comparison. L-O. Human T cells interacting with immobilized recombinant BBB adhesion molecules. L. Raw fluorescent image frame, thresholding-

based segmentation, and tracking results. M. Crawling vs probing behavior distribution. N. X and Y relative displacement O. Crawling vs probing speed comparison.

Scale bar 50 µm. Statistical tests are performed with the Mann-Whitney U test.

506

507 **Discussion**

508 In this study, we have developed the under-flow migration tracker (^{UFM}Track) framework. It
509 consists of independent modules and allows for segmentation (Figure 2), tracking (Figure 3), and
510 motility analysis of immune cells, migrating on, across, and below (Figure 1D) the monolayer of brain
511 microvascular endothelial cells under physiological flow in vitro. The developed method relies
512 exclusively on phase-contrast imaging data (Figure 1B). Therefore, it does not require establishing
513 fluorescent labels of the migrating immune cell population to be studied, avoids potential photo-
514 toxicity to be considered for fluorescent imaging modalities (37–39), and is thus the preferred choice
515 for analyzing the trafficking of sensitive cell types. T-cell segmentation and prediction of the
516 transmigrated T-cell areas are performed using a custom 2D+T U-Net-like convolutional neural
517 network. It enables reliable segmentation of T cells both above and below the pMBMEC monolayer.
518 The existing particle and cell tracking toolkits consider migration of one cell type and thus are not
519 suitable for the detection of distinct migration regimes and cell interactions (23–25,28).
520 Furthermore, to our knowledge, none of the existing algorithms consider migration under the flow
521 causing rapid cell displacement. The tracking of T-cell interactions with the pMBMECs during all
522 migration regimes under physiological flow required designing a new tracking algorithm considering
523 rapid T-cell appearance, disappearance, and displacement in the field of view caused by the flow.
524 We have also developed approaches that resolve track intersections, i.e., identifying track segments
525 corresponding to the same T cell before and after under-segmented track regions, which are
526 inevitable during T-cell migration. By establishing the detection of T-cell crawling, probing,
527 transmigration, and accelerated movement combined with reliable T-cell tracking, we have enabled

528 the in-depth analysis of distinct migration regimes on a cell-by-cell basis. By reducing the dataset
529 analysis time by a factor of 5, UFMTrack allows for performing a thorough analysis of 10 experiments
530 that a researcher can carry out in one day within one day of machine-time. We have demonstrated
531 that the automated analysis performs on par with manual analysis while improving accuracy and
532 eliminating experimenter bias, and enables scalability of flow-based immune cell migration
533 experiments by reducing the analysis cost and lifting the burden of time-consuming manual analysis.

534 In this work, we have demonstrated the applicability of the developed framework to the analysis
535 of the multi-step extravasation of $CD4^+$ and $CD8^+$ T cells across non-stimulated or cytokine-
536 stimulated pMBMEC monolayers under physiological flow. We have also demonstrated that the
537 developed framework allows for automated analysis of T-cell behavior statistics and motility
538 parameters of distinct T-cell migration regimes. Results of the automated analysis of $CD4^+$ T-cell
539 behavioral statistics performed with UFMTrack are in agreement with previous studies using manual
540 data analysis (Figure 4B) (14). The automated analysis of datasets of $CD8^+$ T-cell migration has shown
541 comparable performance with manual analysis performed by one experimenter with four years of
542 analysis experience and three less-experienced experimenters. At the same time, the variance of the
543 results obtained manually showed significant experimenter bias that the automated analysis
544 eliminated (Figure 5F). Additionally, the automated analysis allowed for in-depth analysis of all T-cell
545 migration categories and precise evaluation of T-cell motility parameters, which was not achieved by
546 manual T-cell tracking, even by the most experienced user.

547 We have further demonstrated the applicability of the UFMTrack framework to the analysis of
548 different cell types (BMDM, PBMC), species (human-derived T cells, HBMEC, and EECM BMEC) as
549 well as tracking and analysis of cell migration imaged using the fluorescent imaging modality. In all
550 cases, the cells could be successfully segmented and tracked, and the cell migration analysis was
551 performed on a cell-by-cell basis. The main challenge for the system is reliable segmentation of the T
552 cells and the transmigrated T cells. In the case of HBMEC the monolayer has a dotted pattern unlike

553 the rather smooth pMBMEC. This leads to more false positives in the T-cell segmentation at the level
554 of individual frames, which nonetheless could be efficiently filtered at the level of cell tracking. In the
555 case of the BMDMs, since they have significantly different appearances during transmigration from
556 the T cells, reliable transmigration detection was not obtained. This prevents the system from
557 quantifying the transmigration statistics of the BMDMs, yet the cell detection and thus motility
558 parameter evaluation of BMDMs was successful (Figure 6 D-F). For all the other analyzed cell types,
559 both the cell segmentation and transmigration detection model trained on the annotated $CD4^+$ T
560 cells also produced transmigration maps of sufficient quality for reliable transmigration detection.
561 The framework was able to successfully detect the cells of sizes that differ by almost a factor of two
562 (Supplementary Figure 7). This demonstrates, that simply by discriminating cells by size, it is possible
563 to extend ^{UFM}Track to study interaction of several types of immune cells migrating on top of a cellular
564 monolayer under flow and imaged by phase contrast.

565 Quantifying the fraction of transmigrated T cells is crucial for studying the molecular mechanisms
566 governing the infiltration of autoaggressive T cells across the BBB into the CNS parenchyma and the
567 immune surveillance. The role of specific endothelial or T-cell adhesion molecules in influencing the
568 dynamic interactions of T cells with pMBMECs can, e.g., be probed by quantifying the ratio of T-cell
569 crawling behavior to T-cell probing (Figure 6M) (14,40,41). The analysis procedure established in the
570 ^{UFM}Track framework is flexible and can be easily extended to evaluate further properties of the
571 migrating cells. For example, the number of times a T cell interrupts its crawling regime by switching
572 to short probing behavior on the endothelium can be evaluated, thus providing information on the
573 distribution of “hot spots” on the endothelium. Additionally, experiment scalability and the analysis
574 on a cell-by-cell basis enable the search for distinct populations of T-cells, e.g., according to the
575 distribution of probing to crawling behavioral ratios. The strength of T-cell adhesion to the
576 endothelium can be probed with the developed framework using the measure of T-cell detachment
577 rate and the distribution of the previously overlooked T-cell accelerated movement occurrences and
578 accelerated movement speed. Finally, the possibility of quantifying the motility parameters of the

579 transmigrated T cells enables future studies involving multilayer in vitro BBB models that include the
580 vascular basement membrane in addition to mural cells such as pericytes and astrocytes mimicking
581 the entire neurovascular unit.

582 While in this work we have focused primarily on the analysis of mouse T cells interacting with
583 pMBMEC under flow or other immune cells interacting with the endothelial monolayer, the methods
584 we present establish a foundation for a broad range of studies involving in vitro under-flow studies
585 of immune cell trafficking. The tracking algorithm and motility analysis developed in the ^{UFM}Track
586 framework are also directly applicable to the analysis of immune cell interactions with recombinant
587 BBB adhesion molecules under flow. In this case, either phase-contrast or epi-fluorescent imaging
588 can be employed when studying fluorescently labeled immune cells, as demonstrated. The T-cell
589 segmentation based on deep neural networks can be applied to studies of the trafficking of other
590 immune cell subsets on and across the pMBMEC monolayer. We demonstrated the successful
591 application of the ^{UFM}Track to cells with significantly different appearances, such as the HBMEC
592 cellular monolayers.

593 We make UFMTrack available to the community to build upon it for addressing their specific
594 research questions. The modularity of the framework simplifies the adaptation to analysis of
595 different cell types. The application to immune cell trafficking across other endothelial monolayers,
596 including those from different species or vascular beds as well as lymphatic endothelial cells where
597 the cell appearance is drastically different from the ones demonstrated here, is possible but requires
598 fine-tuning of the trained segmentation model. While training the models presented here required a
599 large dataset of annotated T-cell masks, and transmigration masks, this can be largely avoided for
600 future development. Future models can be developed more efficiently by leveraging our existing
601 annotated dataset of T-cell migration on the pMBMECs while employing transfer learning
602 approaches in a multitask framework with weak supervision and fluorescent labels as auxiliary
603 learning targets to adapt the model for the segmentation of cells with different appearances. This

604 can be further improved by adopting self-supervised contrastive or masked learning methods, which
605 have demonstrated significant advancements in model pretraining in recent years (42–45). This is
606 the subject of our future studies. The framework could be employed in combination of other
607 methods, e.g. by incorporating fluorescently labeled endothelial adherens junctions one could
608 differentiate the trans- from the paracellular transmigration in the migrating cells. In this case the
609 transmigration locations detected by the ^{UFM}Track framework could be automatically extracted for
610 analysis. One could employ the tracking under flow implemented in the ^{UFM}Track framework for
611 tracking the immune cells migrating on the vascular wall *in vivo* to capture the accelerated
612 movement of cells. By sharing the data and open-source code of the ^{UFM}Track framework, i.e., the
613 training data used for the segmentation model training, trained models, as well as the model
614 architecture, and full under-flow T-cell tracking and migration analysis pipeline, we hope to
615 encourage the community to pursue these developments to advance the field.

616 One current limitation of the method is the performance reduction of the T-cell tracking when
617 the density of migrating T cells significantly increases (>250 cells/dataset). Thus, the recommended T
618 cell concentration is about 100-150k/ml. However, to avoid non-physiological interactions between
619 migrating T cells and T cell clumping, the T-cell density should be kept at moderate levels anyway.
620 Additionally, analyzing data from 8 stitched FoVs allows for obtaining comparable statistics. The
621 current analysis of the behavioral statistics quantifies the fraction of different T-cell migration
622 regimes with respect to the number of adhered cells instead of the total T-cell count passing through
623 the microfluidic device. While the number of fast-moving T cells during the accumulation phase
624 cannot be directly counted using the imaging modality employed here, it can be estimated indirectly
625 from the imaging data with additional calibration experiments and a dedicated machine learning
626 model. Another limitation is that currently, we do not consider dividing immune cells. While cell
627 division events happen rarely (<1% of T cells) and are not primary events for the study of immune
628 cell interaction with the BBB model, the modular architecture of our framework will facilitate future
629 extension to detect cell division.

630 By enabling experiment scalability, unbiased analysis with advanced accuracy, and an in-depth
631 analysis of large datasets of T-cell dynamics under flow, the computational and analytical framework
632 presented here contributes to the 3R principle when studying the interaction of cells derived from
633 animal models by reducing the number of animals to be sacrificed. ^{UFM}Track can be employed for
634 fundamental research of the molecular mechanisms governing immune cell trafficking across a range
635 of vascular beds, screening of pharmaceutical treatments, as well as for personalized medicine
636 based on the evaluation of treatment efficacy on patient-derived T-cell migration behavior on
637 patient-derived endothelial monolayers. One can furthermore envisage that ^{UFM}Track can be suitable
638 to study cancer cell metastasis across different endothelial cell monolayers. Eventually, the
639 developed framework can be extended to real-time operation during image acquisition. Combined
640 with transgenic photo-convertible immune cells allowing for the photoconversion of immune cells
641 according to their behavior will allow for subsequent fluorescent cell sorting and scRNA-Seq analysis.
642 Such advanced studies are needed to reveal the role of genetic differences governing T-cell
643 migration regimes.
644
645

646 Materials and Methods

647 1. pMBMEC cell culture

648 Primary mouse brain microvascular endothelial cells (pMBMECs) were isolated from 8-12 weeks
649 old C57BL/6J WT mice and cultured exactly as described before (12,46). Intact monolayers were
650 stimulated or not with 10 ng/mL of recombinant mouse TNF, 20 ng/mL of recombinant mouse IL1-β
651 for, or 5ng/mL recombinant mouse TNF + 100 U/mL recombinant mouse IFN-γ 16-24 hours prior to
652 the assays as previously described (32).

653

654 2. Human brain microvascular endothelial cells

655 Human brain microvascular endothelial cells (HBMEC) were kindly provided by Prof. Nicholas
656 Schwab (University of Münster, Germany). They were cultured to confluency on speed coating
657 solution coated µ-Dishes (35 mm, low, iBidi) for 2 days as previously described (32).

658

659 3. Extended endothelial culture method—brain microvascular endothelial cell-like cells

660 The Extended Endothelial Cell Culture Method (EECM) was used to differentiate human induced
661 pluripotent stem cells (hiPSCs) to brain microvascular endothelial cell (BMEC)-like cells were
662 employed as a human in vitro model of the BBB. In brief, hiPSCs from one healthy control (HC) (cell
663 line ID: LNISi002-B) were established from erythroblasts in the laboratory of Renaud DuPasquier
664 (University of Lausanne, Switzerland). EECM-BMEC-like cells were cultured to confluency on collagen
665 IV and fibronectin-coated µ-Dishes (35 mm, low, iBidi) for 2 days (36).

666

667 4. T cell and hPBMC preparation

668 Naïve $CD4^+$ and $CD8^+$ T-cell isolation: Peripheral lymph nodes and spleens from 2D2 and OT-I
669 C57BL/6J mice were harvested, and single-cell suspensions were obtained by homogenization and
670 filtration through a sterile 100 μm nylon mesh. A second filtration was applied after erythrocyte lysis
671 (0.83% NH4Cl, Tris-HCl). 2D2 and OT-I cells were isolated respectively with magnetic $CD4^+$ and $CD8^+$ T
672 cell selection beads (EasySep, STEMCELL Technologies).

673 In vitro activation of naïve $CD8^+$ T cells: OT-I $CD8^+$ T cells were activated as described before
674 (13,41). Activated $CD8^+$ T cells were cultured in IL-2-containing media for 3 days post-activation.

675 In vitro activation of naïve $CD4^+$ T cells: 2D2 $CD4^+$ T cells were activated as described before (32).
676 Activated $CD4^+$ T cells were cultured in IL-2-containing media for 24 additional hours.

677 hPBMC were isolated from buffy coats of healthy donors by Ficoll-Paque™ Plus (Cytiva) density
678 gradient and were frozen and stored in a liquid nitrogen tank until use as previously described in
679 (36).

680 Human $CD4^+$ T cells were isolated by employing a $CD4^+$ T cells isolation kit (Miltenyi Biotec kit)
681 following the provider's instructions. Subsequently, effector/memory $CD4^+$ T cells were sorted by
682 Fluorescence-Activated Cell Sorting (FACS) into different Th subsets according to their specific
683 surface expression of chemokine receptors ($CCR6^-CXCR3^+CCR4^-$ for Th1; $CCR6^+CXCR3^+CCR4^-$ for
684 Th1*; $CCR6^-CXCR3^-CCR4^+$ for Th2; $CCR6^+CXCR3^-CCR4^+$ for Th17) and expanded as previously
685 described (1,33,40,47–49).

686

687 5. BMDM preparation

688 BMDMs were prepared as described in (Berve et al., manuscript in preparation). In brief, the
689 mouse bone marrow was harvested and washed through a 100 µm nylon mesh. After 7 days of cell
690 culture were plated in a density of 17-20 × 10^6 cells/mL in BMDM medium supplemented with
691 5ng/mL of recombinant mouse macrophage colony stimulating factor (mCSF, R&D Biosystems,

692 Minneapolis, USA, 416-ML-500) onto non-treated 100mm tissue culture Petri dishes (Greiner Bio-
693 One, St. Gallen, Switzerland) for 7 days at 37°C and 5% CO_2 the cells were harvested by incubation
694 with 0.05% Trypsin.

695

696 6. T cell binding assays under physiological flow conditions

697 For live-cell imaging of T-cell interaction with recombinant BBB cell adhesion molecules under the
698 physiological flow condition, µ-Dishes (35 mm, low, iBidi) were coated with 1.54 µg/mL human
699 recombinant VCAM-1 (Biolegend) and/or 1.14 µg/mL human recombinant ICAM-1 (R&D system) in
700 DPBS for 1 h at 37°C and blocked with 1.5% (v/v) bovine serum albumin (Sigma-Aldrich) in DPBS
701 overnight at 4°C.

702 CMFDA prelabelled Th cells were incubated with the isotype control antibody (30 µg/mL) for 30
703 minutes at 37°C (8% CO_2) prior to imaging (exact antibody concentrations are illustrated in the figure
704 legend). The cells were subsequently perfused on top of the pre-coated dishes at a concentration of
705 10^6/mL in MAM as previously described (12,36).

706

707 7. In vitro under-flow T-cell migration assay

708 We studied the multi-step T-cell migration across monolayers of primary mouse brain
709 microvascular endothelial cells (pMBMECs) in a custom made microfluidic device under physiological
710 flow by in vitro live-cell imaging according to the previously established procedure (14,32). The
711 custom-made flow chamber was described in depth before (11,46). The flow chamber was placed on
712 top of the pMBMECs, previously cultured in Ibidi µ-Dish to confluency, and connected to the flow
713 system filled with migration assay medium (MAM) (12). During the accumulation phase, T cells at a
714 concentration between 55k/mL and 166k/mL were perfused on top for 5 minutes under low shear
715 stress of 0.1 dynes/cm^2, allowing them to settle on top of the pMBMEC monolayer. We used lower

716 T-cell concentration compared to previous studies to enable automated T-cell interaction analysis.
717 Afterward, the flow was increased to physiological levels with a flow shear stress of 1.5 dynes/cm^2 to
718 study post-arrest T-cell behavior on pMBMECs for 27 minutes (Figure 1A, B).

719

720 8. Data acquisition

721 The timelapse imaging was performed during both accumulation and physiological flow phases
722 using phase-contrast imaging at a framerate of 6 frames/minute or 12 frames/minute, subsampled
723 to 6 frames/minute and resolution of 0.629 µm/pixel with a 10x objective. In this modality the
724 acquired images are gray scale, and the T cells, especially after the migration across the pMBMEC
725 monolayer, have a similar appearance to the pMBMECs, making the T-cell segmentation task very
726 challenging (Figure 1C). The data was acquired in tiles of 870 × 650 µm^2 (1389 × 1041 pixels) with an
727 overlap of 100 µm, leading to a total acquired image area of 3170 × 1220 µm^2. For each experiment,
728 the dataset consists of 30 timeframes of T-cell accumulation and 162 timeframes of dynamic T-cell
729 interactions with the pMBMEC monolayer under physiological flow. The timestep between
730 sequential timeframes for each tile is 10 s. The total acquired area is thus limited by the acquisition
731 speed or by the flow chamber size.

732 The HBMEC dataset was acquired as previously described (36). In brief, 2 tiles were acquired of
733 total size 3891 × 1504 pixels with pixel size 0.69 µm and framerate 6 frames/minute. The
734 accumulation phase was 4 minutes, and the physiological flow phase was 5 minutes.

735 The BMDM dataset was acquired similarly to the T cell interacting with the pMBMEC datasets. In
736 brief, one tile was acquired of size of 2048 × 1504 or 1388 × 1040 pixels with pixel size 0.69 or
737 0.629 µm and framerate 6 frames/minute. The accumulation phase lasted 6 minutes, and the
738 physiological flow phase was 25 minutes.

739 The EECM-BMEC dataset was acquired as previously described (36). In brief, 2 tiles were acquired
740 of total size 3892 × 1504 or 2638 × 1048 pixels with pixel size 0.69 or 0.629 µm and framerate
741 6 frames/minute.

742 The dataset of human T cells on immobilized recombinant BBB adhesion molecules was acquired
743 as previously described (36). In brief, 2 tiles were acquired of total size 3891 × 1504 pixels with pixel
744 size 0.69 µm and framerate 6 frames/minute. The accumulation phase was 4 minutes, and the
745 physiological flow phase was 5 minutes. In this dataset, there is only one compartment, thus
746 excluding any transmigration of the T cells. We, therefore, have employed the preprocessed
747 fluorescent images instead of the cell probability map and transmigration map produced by the
748 segmentation neural network. In this case, the centroids are defined as local maxima localized on
749 the preprocessed fluorescent images. The fluorescent images were preprocessed first by performing
750 Gaussian blur filtering in 2D with a standard deviation of 0.75. Next, thresholding was applied to
751 eliminate the background noise, clipping high brightness values (color values with abundance <0.3%
752 of threshold abundance), scaling to 0-255 8 bit, and saving in a lossless format. Finally, the 2 tiles
753 were stitched together by matching the integrated color distribution in the X direction in the
754 overlapping area.

755

756 9. Manual analysis of T-cell migration

757 Manual cell analysis and tracking were performed according to the previously established
758 procedure using ImageJ software (ImageJ software, National Institute of Health, Bethesda, MD, USA)
759 (13). The number of arrested T cells was thus counted at timeframe 33 of the subset. The behavior
760 of arrested T cells was defined and expressed as fractions of arrested T cells set to 100% as follows:

761 - T cells that detached during the observation time ("detached")
762 - T cells that migrated out of the FoV detached during the observation time ("out of FoV")
763 - T cells that continuously crawled on the pMBMEC monolayer ("crawling")

764 • T cells that remained in the same location (displacement less than twice the cell size) while
765 actively interacting with the pMBMEC monolayer ("probing")
766 • T cells that crossed the pMBMEC monolayer with or without prior crawling ("crawling full
767 transmigration" and "probing full transmigration"). The event of T-cell transmigration across the
768 pMBMECs monolayer became obvious due to the change of appearance of the transmigrated part of
769 the T cells from phase bright (on top of the pMBMECs monolayer) to phase dark.
770 • T cells that partially crossed the pMBMEC monolayer, then retracted the protrusions and
771 continued to migrate above the monolayer ("crawling uncompleted transmigration" and "probing
772 uncompleted transmigration").
773
774 10. ^{UFM}Track performance evaluation

775 The inference of T cell masks and transmigration masks was performed on a dual-CPU Intel(R)
776 Xeon(R) CPU E5-2670 v3 @ 2.30GHz, 256GB RAM node equipped with 8 Graphical Processing Units
777 (GPU) NVIDIA GeForce GTX TITAN X / GeForce GTX 1080. Frame alignment and segmentation were
778 performed on an Intel(R) Core(TM) CPU i7-4771 @ 3.50GHz, 32GB RAM workstation with NVIDIA
779 GeForce GTX TITAN GPU. Cell tracking was performed on a dual-CPU Intel(R) Xeon(R) CPU E5-2643
780 v2 @ 3.50GHz, 256GB RAM workstation.

781 11. Performance analysis.

782 The statistical tests are performed with the Mann-Whitney U test. Performance of the
783 segmentation models was evaluated based on the pixel classification metrics evaluated using the
784 scikit-learn library (50). Specifically, the Average Precision is evaluated on the test set as the area
785 under the Precision-Recall curve, as the weighted mean of precisions achieved at each threshold,
786 with the change in recall from the previous threshold used as the weight. The segmentation
787 thresholds for the cell mask and the transmigrated cell mask predictions were selected to maximize
788 the F1 score.

Acknowledgments

We thank Kristina Berve for providing BMDM datasets for analysis with the ^{UFM}Track. We owe sincere thanks to Dr. James McGrath and Danial Ahmad (Rochester University, NY, USA) for their detailed and insightful feedback on our manuscript. This work was supported by an UniBe ID Grant to MV, BE, and AA and the Microscopy Imaging Center (MIC) of the University of Bern.

Data Availability

The source code for the T-cell segmentation models, data preprocessing, training, performance evaluation, and inference scripts are available on GitHub at https://github.com/neworldemancer/UFMSegm. This repository also contains win64 binaries used for the watershed-based segmentation of the predicted T cell probability maps and transmigration probability maps.

The source code for the under-flow T-cell tracking and migration analysis, along with the scripts used for performance evaluation of the framework, is available on GitHub at https://github.com/neworldemancer/UFMTrack.

The training phase-contrast data with manual annotations, the reference datasets for histogram normalization, and trained models are available on Zenodo: [http://doi.org/10.5281/zenodo.7489557].

The datasets used for evaluation of our framework are available on Zenodo: [http://doi.org/10.5281/zenodo.7489972, http://doi.org/10.5281/zenodo.7489984, http://doi.org/10.5281/zenodo.7489996, http://doi.org/10.5281/zenodo.7490012, http://doi.org/10.5281/zenodo.7490020, http://doi.org/10.5281/zenodo.7490029].

812

813 References

814 1. Nishihara H, Soldati S, Mossu A, Rosito M, Rudolph H, Muller WA, et al. Human CD4+ T cell
815 subsets differ in their abilities to cross endothelial and epithelial brain barriers in vitro. Fluids
816 Barriers CNS. 2020 Feb 3;17(1):1–18.

817 2. Marchetti L, Engelhardt B. Immune cell trafficking across the blood-brain barrier in the
818 absence and presence of neuroinflammation. Vascular Biology [Internet]. 2020 Apr 10 [cited
819 2022 Oct 28];2(1):H1–18. Available from:
820 https://vb.bioscientifica.com/view/journals/vb/2/1/VB-19-0033.xml

821 3. Nourshargh S, Alon R. Leukocyte Migration into Inflamed Tissues. Immunity. 2014 Nov
822 20;41(5):694–707.

823 4. Nourshargh S, Hordijk PL, Sixt M. Breaching multiple barriers: leukocyte motility through
824 venular walls and the interstitium. Nature Reviews Molecular Cell Biology 2010 11:5. 2010
825 May;11(5):366–78.

826 5. Engelhardt B, Vajkoczy P, Weller RO. The movers and shapers in immune privilege of the CNS
827 [Internet]. Vol. 18, Nature Immunology. Nature Publishing Group; 2017 [cited 2019 May 3]. p.
828 123–31. Available from: http://www.nature.com/articles/ni.3666

829 6. Bartholomäus I, Kawakami N, Odoardi F, Schläger C, Miljkovic D, Ellwart JW, et al. Effector T
830 cell interactions with meningeal vascular structures in nascent autoimmune CNS lesions.
831 Nature 2009 462:7269. 2009 Oct 14;462(7269):94–8.

832 7. Lyck R, Engelhardt B. Going Against the Tide – How Encephalitogenic T Cells Breach the
833 Blood-Brain Barrier. J Vasc Res. 2012 Oct;49(6):497–509.

834 8. Dias MC, Quesada AO, Soldati S, Bösch F, Gruber I, Hildbrand T, et al. Brain endothelial
835 tricellular junctions as novel sites for T cell diapedesis across the blood-brain barrier. J Cell
836 Sci. 2021 Apr 1;134(8).

837 9. Steinman L, Zamvil SS. Virtues and pitfalls of EAE for the development of therapies for
838 multiple sclerosis. Trends Immunol. 2005;26(11):565–71.

839 10. Singer BA. The role of natalizumab in the treatment of multiple sclerosis: benefits and risks.
840 Ther Adv Neurol Disord. 2017 Sep 1;10(9):327–36.

841 11. Lyck R, Nishihara H, Aydin S, Soldati S, Engelhardt B. Modeling Brain Vasculature Immune
842 Interactions In Vitro. Cold Spring Harb Perspect Med [Internet]. 2023 Sep 12 [cited 2023 Jul
843 19];13(9):a041185. Available from:
844 http://perspectivesinmedicine.cshlp.org/lookup/doi/10.1101/cshperspect.a041185

845 12. Steiner O, Coisne C, Cecchelli R, Boscacci R, Deutsch U, Engelhardt B, et al. Differential Roles
846 for Endothelial ICAM-1, ICAM-2, and VCAM-1 in Shear-Resistant T Cell Arrest, Polarization,
847 and Directed Crawling on Blood–Brain Barrier Endothelium. The Journal of Immunology. 2010
848 Oct 15;185(8):4846–55.

13. Rudolph H, Klopstein A, Gruber I, Blatti C, Lyck R, Engelhardt B. Postarrest stalling rather than crawling favors CD8+ over CD4+ T-cell migration across the blood–brain barrier under flow in vitro. Eur J Immunol [Internet]. 2016 Sep 1 [cited 2020 Mar 9];46(9):2187–203. Available from: https://onlinelibrary.wiley.com/doi/full/10.1002/eji.201546251

14. Abadier M, Jahromi NH, Alves LC, Boscacci R, Vestweber D, Barnum S, et al. Cell surface levels of endothelial ICAM-1 influence the transcellular or paracellular T-cell diapedesis across the blood–brain barrier. 2015 Apr 1 [cited 2019 Apr 19];45(4):1043–58. Available from: http://doi.wiley.com/10.1002/eji.201445125

15. Shulman Z, Shinder V, Klein E, Grabovsky V, Yeger O, Geron E, et al. Lymphocyte Crawling and Transendothelial Migration Require Chemokine Triggering of High-Affinity LFA-1 Integrin. Immunity. 2009 Mar 20;30(3):384–96.

16. Arts JJG, Mahlandt EK, Grönloh MLB, Schimmel L, Noordstra I, Gordon E, et al. Endothelial junctional membrane protrusions serve as hotspots for neutrophil transmigration. Elife. 2021 Aug 1;10.

17. He K, Gkioxari G, Dollár P, Girshick R. Mask R-CNN. IEEE Trans Pattern Anal Mach Intell [Internet]. 2017 Mar 20 [cited 2024 Jul 23];42(2):386–97. Available from: https://arxiv.org/abs/1703.06870v3

18. Wang CY, Bochkovskiy A, Liao HYM. YOLOv7: Trainable bag-of-freebies sets new state-of-the-art for real-time object detectors. 2022 Jul 6 [cited 2024 Jul 23];7464–75. Available from: https://arxiv.org/abs/2207.02696v1

19. Carion N, Massa F, Synnaeve G, Usunier N, Kirillov A, Zagoruyko S. End-to-End Object Detection with Transformers. Lecture Notes in Computer Science (including subseries Lecture Notes in Artificial Intelligence and Lecture Notes in Bioinformatics) [Internet]. 2020 May 26 [cited 2024 Jul 23];12346 LNCS:213–29. Available from: https://arxiv.org/abs/2005.12872v3

20. Schmidt U, Weigert M, Broaddus C, Myers G. Cell Detection with Star-convex Polygons. Lecture Notes in Computer Science (including subseries Lecture Notes in Artificial Intelligence and Lecture Notes in Bioinformatics) [Internet]. 2018 Jun 9 [cited 2024 Jul 23];11071 LNCS:265–73. Available from: https://arxiv.org/abs/1806.03535v2

21. Ronneberger O, Fischer P, Brox T. U-Net: Convolutional Networks for Biomedical Image Segmentation. 2015 May 18 [cited 2017 Oct 25]; Available from: http://arxiv.org/abs/1505.04597

22. Stringer C, Wang T, Michaelos M, Pachitariu M. Cellpose: a generalist algorithm for cellular segmentation. Nature Methods 2020 18:1 [Internet]. 2020 Dec 14 [cited 2024 Jul 23];18(1):100–6. Available from: https://www.nature.com/articles/s41592-020-01018-x

23. Allan DB, Caswell T, Keim NC, van der Wel CM, Verweij RW. Trackpy. 2021 Apr 13 [cited 2022 Oct 29]; Available from: https://zenodo.org/record/4682814

24. Tsai HF, Gajda J, Sloan TFW, Rares A, Shen AQ. Usiigaci: Instance-aware cell tracking in stain-free phase contrast microscopy enabled by machine learning. SoftwareX. 2019 Jan 1;9:230–7.

25. Ershov D, Phan MS, Pylvänäinen JW, Rigaud SU, Le Blanc L, Charles-Orszag A, et al. TrackMate 7: integrating state-of-the-art segmentation algorithms into tracking pipelines. Nature

Methods 2022 19:7 [Internet]. 2022 Jun 2 [cited 2022 Oct 29];19(7):829–32. Available from: https://www.nature.com/articles/s41592-022-01507-1

26. Rueden CT, Schindelin J, Hiner MC, DeZonia BE, Walter AE, Arena ET, et al. ImageJ2: ImageJ for the next generation of scientific image data. BMC Bioinformatics [Internet]. 2017 Nov 29 [cited 2024 Jul 4];18(1):1–26. Available from: https://link.springer.com/articles/10.1186/s12859-017-1934-z

27. Holme B, Bjørnerud B, Pedersen NM, de la Ballina LR, Wesche J, Haugsten EM. Automated tracking of cell migration in phase contrast images with CellTraxx. Scientific Reports 2023 13:1 [Internet]. 2023 Dec 27 [cited 2024 Jul 23];13(1):1–20. Available from: https://www.nature.com/articles/s41598-023-50227-9

28. Ulicna K, Vallardi G, Charras G, Lowe AR. Automated Deep Lineage Tree Analysis Using a Bayesian Single Cell Tracking Approach. Front Comput Sci. 2021 Oct 20;3:92.

29. Abadi M, Barham P, Chen J, Chen Z, Davis A, Dean J, et al. TensorFlow: A system for large-scale machine learning.

30. Schiegg M, Hanslovsky P, Kausler BX, Hufnagel L, Hamprecht FA. Conservation Tracking. 2013;

31. Perron L, Furnon V. OR-Tools [Internet]. Available from: https://developers.google.com/optimization/

32. Haghayegh Jahromi N, Marchetti L, Moalli F, Duc D, Basso C, Tardent H, et al. Intercellular Adhesion Molecule-1 (ICAM-1) and ICAM-2 Differentially Contribute to Peripheral Activation and CNS Entry of Autoaggressive Th1 and Th17 Cells in Experimental Autoimmune Encephalomyelitis. Front Immunol. 2020 Jan 14;10:3056.

33. Mossu A, Rosito M, Khire T, Li Chung H, Nishihara H, Gruber I, et al. A silicon nanomembrane platform for the visualization of immune cell trafficking across the human blood–brain barrier under flow. Journal of Cerebral Blood Flow and Metabolism. 2019 Mar 1;39(3):395–410.

34. Clockify. Clockify™ - 100% FREE Time Tracking Software [Internet]. 2022 [cited 2022 Oct 23]. Available from: https://clockify.me/

35. Nishihara H, Gastfriend BD, Kasap P, Palecek SP, Shusta E V., Engelhardt B. Differentiation of human pluripotent stem cells to brain microvascular endothelial cell-like cells suitable to study immune cell interactions. STAR Protoc. 2021 Jun 18;2(2).

36. Soldati S, Bär A, Vladymyrov M, Glavin D, McGrath JL, Gosselet F, et al. High levels of endothelial ICAM-1 prohibit natalizumab mediated abrogation of CD4+ T cell arrest on the inflamed BBB under flow in vitro. J Neuroinflammation. 2023 May 23;20(1):123.

37. Jae Oh D, Min Lee G, Francis K, Palsson BO. Phototoxicity of the Fluorescent Membrane Dyes PKH2 and PKH26 on the Human Hematopoietic KG1a Progenitor Cell Line.

38. Saetzler RK, Jallo J, Lehr HA, Philips CM, Vasthare U, Arfors KE, et al. Intravital Fluorescence Microscopy: Impact of Light-induced Phototoxicity on Adhesion of Fluorescently Labeled Leukocytes. The Journal of Histochemistry & Cytochemistry. 1997;45(4):505–13.

39. Purschke M, Rubio N, Held KD, Redmond RW. Phototoxicity of Hoechst 33342 in time-lapse fluorescence microscopy. Photochem Photobiol Sci. 2010;9(12):1634–9.

928 40. Wimmer I, Tietz S, Nishihara H, Deutsch U, Sallusto F, Gosselet F, et al. PECAM-1 stabilizes
929 blood-brain barrier integrity and favors paracellular T-cell diapedesis across the blood-brain
930 barrier during neuroinflammation. Front Immunol. 2019 Apr 5;10(APR):447986.

931 41. Aydin S, Pareja J, Schallenberg VM, Klopstein A, Gruber T, Page N, et al. Antigen recognition
932 detains CD8+ T cells at the blood-brain barrier and contributes to its breakdown. Nature
933 Communications 2023 14:1 [Internet]. 2023 May 30 [cited 2023 Jul 31];14(1):1–20. Available
934 from: https://www.nature.com/articles/s41467-023-38703-2

935 42. Caron M, Touvron H, Misra I, Jegou H, Mairal J, Bojanowski P, et al. Emerging Properties in
936 Self-Supervised Vision Transformers. Proceedings of the IEEE International Conference on
937 Computer Vision [Internet]. 2021 Apr 29 [cited 2024 Jun 24];9630–40. Available from:
938 https://arxiv.org/abs/2104.14294v2

939 43. Archit A, Nair S, Khalid N, Hilt P, Rajashekar V, Freitag M, et al. Segment Anything for
940 Microscopy. bioRxiv [Internet]. 2023 Aug 22 [cited 2024 Jun 24];2023.08.21.554208. Available
941 from: https://www.biorxiv.org/content/10.1101/2023.08.21.554208v1

942 44. Kraus O, Kenyon-Dean K, Saberian S, Fallah M, McLean P, Leung J, et al. Masked
943 Autoencoders for Microscopy are Scalable Learners of Cellular Biology. 2024 Apr 16 [cited
944 2024 Jun 24]; Available from: https://arxiv.org/abs/2404.10242v1

945 45. Xie R, Pang K, Bader GD, Wang B. MAESTER: Masked Autoencoder Guided Segmentation at
946 Pixel Resolution for Accurate, Self-Supervised Subcellular Structure Recognition. In 2023. p.
947 3292–301.

948 46. Coisne C, Lyck R, Engelhardt B. Live cell imaging techniques to study T cell trafficking across
949 the blood-brain barrier in vitro and in vivo. Fluids Barriers CNS [Internet]. 2013 Jan 21 [cited
950 2020 Mar 9];10(1):7. Available from: http://www.ncbi.nlm.nih.gov/pubmed/23336847

951 47. Engen SA, Rukke HV, Becattini S, Jarrossay D, Blix IJ, Petersen FC, et al. The Oral Commensal
952 Streptococcus mitis Shows a Mixed Memory Th Cell Signature That Is Similar to and Cross-
953 Reactive with Streptococcus pneumoniae. PLoS One. 2014 Aug 13;9(8):e104306.

954 48. Sallusto F, Lenig D, Mackay CR, Lanzavecchia A. Flexible Programs of Chemokine Receptor
955 Expression on Human Polarized T Helper 1 and 2 Lymphocytes. Journal of Experimental
956 Medicine. 1998 Mar 16;187(6):875–83.

957 49. Zielinski CE, Mele F, Aschenbrenner D, Jarrossay D, Ronchi F, Gattorno M, et al. Pathogen-
958 induced human TH17 cells produce IFN-γ or IL-10 and are regulated by IL-1β. Nature 2012
959 484:7395. 2012 Apr 1;484(7395):514–8.

960 50. Pedregosa F, Varoquaux G, Gramfort A, Michel V, Thirion B, Grisel O, et al. Scikit-learn:
961 Machine Learning in Python. Journal of Machine Learning Research. 2011;12:2825–30.

962

963

964